

# Optimal Transport, CycleGAN, and Penalized LS for Unsupervised Learning in Inverse Problems \*

Byeongsu Sim<sup>†</sup>, Gyutaek Oh<sup>‡</sup>, Jeongsol Kim<sup>§</sup>, Chanyong Jung<sup>¶</sup>, and Jong Chul Ye<sup>||</sup>

**Abstract.** The penalized least squares (PLS) is a classic method to inverse problems, where a regularization term is added to stabilize the solution. Optimal transport (OT) is another mathematical framework for computer vision tasks that provides means to transport one measure to another at minimal cost. The cycle-consistent generative adversarial network (cycleGAN) is a recent extension of GAN to learn target distributions with less mode collapsing behavior. Although similar in that no supervised training is required, the algorithms look different, so the mathematical relationship between these approaches is not clear. In this article, we provide an important advance to unveil the missing link. Specifically, we reveal that a cycleGAN architecture is originated from formulating a dual OT problem, by using the consistency constraint of PLS as a regularization term in the primal OT problem. This suggests that cycleGAN can be considered stochastic generalization of classical PLS approaches. Our derivation is so general that various types of cycleGAN architectures can be easily derived by merely changing the transport cost. As proofs of concept, we provide three distinct cycleGAN architecture for various biomedical imaging problems, such as accelerated magnetic resonance imaging (MRI), super-resolution microscopy, and low-dose x-ray computed tomography (CT). Experimental results confirm the efficacy and the flexibility of the theory.

**1. Introduction.** Inverse problems are ubiquitous in computer vision, biomedical imaging, scientific discovery, etc. In inverse problems, a noisy measurement  $y \in \mathcal{Y}$  from an unobserved image  $x \in \mathcal{X}$  is modeled by

$$(1.1) \quad y = \mathcal{H}x + w ,$$

where  $w$  is the measurement noise, and  $\mathcal{H} : \mathcal{X} \mapsto \mathcal{Y}$  is the measurement operator. In inverse problems originating from physics, the measurement operator is usually represented by an integral equation:

$$(1.2) \quad \mathcal{H}x(\mathbf{r}) := \int_{\mathbb{R}^d} h(\mathbf{r}, \mathbf{r}')x(\mathbf{r}')d\mathbf{r}', \quad \mathbf{r} \in \mathcal{D} \subset \mathbb{R}^d, \quad d = 2, 3,$$

where  $h(\mathbf{r}, \mathbf{r}')$  is an integral kernel. Then, the inverse problem is formulated as an estimation problem of the unknown  $x$  from the measurement  $y$ . It is well known that inverse problems are ill-posed. A classical strategy to mitigate the ill-posedness is the penalized least squares (PLS) approach:

$$(1.3) \quad \hat{x} = \arg \min_x c(x; y) := \|y - \mathcal{H}x\|^q + R(x)$$

---

\*Submitted on May 29, 2022.

**Funding:** This work was supported by the National Research Foundation (NRF) of Korea grant NRF-2016R1A2B3008104.

<sup>†</sup>Department of Mathematical Sciences, KAIST, Daejeon, Republic of Korea.

<sup>‡</sup>Department of Bio and Brain Engineering, KAIST, Daejeon, Republic of Korea.

<sup>§</sup>Department of Bio and Brain Engineering, KAIST, Daejeon, Republic of Korea.

<sup>¶</sup>Department of Bio and Brain Engineering, KAIST, Daejeon, Republic of Korea.

<sup>||</sup>Jong Chul Ye is with the Department of Bio and Brain Engineering and Department of Mathematical Sciences, KAIST, Daejeon, Republic of Korea. [jong.ye@kaist.ac.kr](mailto:jong.ye@kaist.ac.kr)

for  $q \geq 1$ , where  $R(x)$  is a regularization (or penalty) function ( $l_1$ , total variation (TV), etc.) [6, 33, 24]. In some inverse problems, the measurement operator  $\mathcal{H}$  is not well defined, so both the unknown operator  $\mathcal{H}$  and the image  $x$  should be estimated.

Recently, deep learning approaches with supervised training have become a mainstream approach for inverse problems thanks to their excellent performance and ultra-fast reconstruction time. In contrast to the PLS, a top-down prior model is not required, and a neural network automatically finds the signal representation in a data-driven manner. For example, in low-dose x-ray computed tomography (CT) denoising problems, a convolutional neural network (CNN) is trained to learn the relationship between the noisy image  $y$  and the matched noiseless (or high-dose) label images  $x$  [19]. In the context of (1.3), the supervised neural network can be understood as directly learning the nonlinear operation  $\hat{x} = \arg \min_x c(x; y)$ . Unfortunately, in many applications, matched label data are not available.

Recently, the generative adversarial network (GAN) has attracted significant attention in the machine learning community by providing a way to generate target data distribution from random distribution [9]. In particular, [2] proposed the so-called Wasserstein GAN (W-GAN), which is closely related to the mathematical theory of optimal transport (OT) [38, 29]. In OT, for two given probability measures supported on the  $\mathcal{X}$  and  $\mathcal{Y}$  spaces, one pays a cost for transporting one measure to another. Then, the minimization of the average transportation cost provides an unsupervised way of learning the transport map between the two measures. Unfortunately, these GAN approaches often generate artificial features due to mode collapsing, so cycle-consistent GAN (cycleGAN) [42], which imposes one-to-one correspondence, has been extensively investigated [18, 22].

Although classical PLS, OT, and cycleGAN share the commonality of unsupervised learning which does not require matched training data, there is no mathematical theory to systematically link these seemingly different approaches. Therefore, one of the main contributions of this paper is to unveil the missing link between these methods. In particular, we reveal that a cycleGAN architecture can be obtained from approximating the Kantorovich's dual formulation of OT problem when the consistency term in PLS is enforced as a regularization term in the primal OT problem. We show that the approximation error goes to zero when the cycle-consistency term approaches to zero during the network training. This framework is so general that various cycleGAN architectures can be easily obtained by merely changing the PLS cost in the primal OT problem.

As proofs of concept, we provide three distinct cycleGAN architectures for unsupervised learning in three physical inverse problems: accelerated MRI, deconvolution microscopy, and low-dose CT reconstruction. The experimental results confirm that the proposed unsupervised learning approaches can successfully provide accurate inversion results without any matched reference.

## 2. Related Works.

**2.1. Optimal Transport (OT).** OT compares two measures in a Lagrangian framework [38, 29]. Formally, we say that  $T : \mathcal{X} \mapsto \mathcal{Y}$  transports  $\mu \in P(\mathcal{X})$  to  $\nu \in P(\mathcal{Y})$ , if

$$(2.1) \quad \nu(B) = \mu(T^{-1}(B)), \quad \text{for all } \nu\text{-measurable sets } B,$$

which is often simply represented by  $\nu = T_{\#}\mu$ , where  $T_{\#}$  is often called the push-forward operator. Monge's original OT problem [38, 29] is then to find a transport map  $T$  that transports  $\mu$  to  $\nu$  at the minimum total transportation cost:

$$\min_T \mathbb{M}(T) := \int_{\mathcal{X}} c(x, T(x)) d\mu(x), \quad \text{subject to } \nu = T_{\#}\mu \quad .$$

Since this is usually computationally expensive due to the nature of combinatorial assignment, Kantorovich relaxed the assumption to consider probabilistic transport that allows mass splitting from a source toward several targets [38, 29]. Specifically, Kantorovich introduced a joint measure  $\pi \in P(\mathcal{X} \times \mathcal{Y})$  and the associated cost  $c(x, y), x \in \mathcal{X}, y \in \mathcal{Y}$  such that the original problem can be relaxed as

$$(2.2) \quad \min_{\pi} \int_{\mathcal{X} \times \mathcal{Y}} c(x, y) d\pi(x, y) \\ \text{subject to } \pi(A \times \mathcal{Y}) = \mu(A), \quad \pi(\mathcal{X} \times B) = \nu(B)$$

for all measurable sets  $A \in \mathcal{X}$  and  $B \in \mathcal{Y}$ . Here, the last two constraints come from the observation that the total amount of mass removed from any measurable set has to be equal to the marginals [38, 29].

One of the most important advantages of Kantorovich formulation is the dual formulation as stated in the following theorem:

**Theorem 2.1 (Kantorovich duality theorem).** [38, Theorem 5.10, p.57-p.59] *Let  $(\mathcal{X}, \mu)$  and  $(\mathcal{Y}, \nu)$  be two Polish probability spaces (separable complete metric space) and let  $c : \mathcal{X} \times \mathcal{Y} \rightarrow \mathbb{R}$  be a continuous cost function, such that  $|c(x, y)| \leq c_{\mathcal{X}}(x) + c_{\mathcal{Y}}(y)$  for some  $c_{\mathcal{X}} \in L^1(\mu)$  and  $c_{\mathcal{Y}} \in L^1(\nu)$ , where  $L^1(\mu)$  denotes a Lebesgue space with integral function with the measure  $\mu$ . Then, there is a duality:*

$$(2.3) \quad \min_{\pi \in \Pi(\mu, \nu)} \int_{\mathcal{X} \times \mathcal{Y}} c(x, y) d\pi(x, y) = \sup_{\varphi \in L^1(\mu)} \left\{ \int_{\mathcal{X}} \varphi(x) d\mu(x) + \int_{\mathcal{Y}} \varphi^c(y) d\nu(y) \right\}$$

$$(2.4) \quad = \sup_{\psi \in L^1(\mu)} \left\{ \int_{\mathcal{X}} \psi^c(x) d\mu(x) + \int_{\mathcal{Y}} \psi(y) d\nu(y) \right\}$$

where

$$\Pi(\mu, \nu) := \{ \pi \mid \pi(A \times \mathcal{Y}) = \mu(A), \quad \pi(\mathcal{X} \times B) = \nu(B) \},$$

and the above maximum is taken over the so-called Kantorovich potentials  $\varphi$  and  $\varphi^c$ , whose  $c$ -transforms are defined as

$$(2.5) \quad \varphi^c(y) := \inf_x (c(x, y) - \varphi(x)), \quad \psi^c(x) := \inf_y (c(x, y) - \psi(y))$$

In the Kantorovich dual formulation, the calculation of  $c$ -transform  $\varphi^c$  is important. In particular, this can be simplified to  $-\varphi$  if  $c(x, y) = \|x - y\|$  and  $\varphi$  is 1-Lipschitz [38].

**2.2. PLS with Deep Learning Prior.** Recently, PLS frameworks using a deep learning prior have been extensively studied [41, 1] thanks to their similarities to the classical regularization theory. The main idea of these approaches is to utilize a pre-trained neural network to stabilize the inverse solution. For example, in model based deep learning architecture (MoDL) [1], the problem can be formulated as

$$(2.6) \quad \min_x c(x; y, \Theta, \mathcal{H}) = \|y - \mathcal{H}x\|^2 + \lambda \|x - Q_\Theta(x)\|^2$$

for some regularization parameter  $\lambda > 0$ , where  $Q_\Theta(x)$  is a pre-trained CNN with the network parameter  $\Theta$  and the input  $x$ . This problem is usually solved in an alternating minimization framework:

$$(2.7) \quad x_{n+1} = \arg \min_x \|y - \mathcal{H}x\|^2 + \lambda \|x - z_n\|^2, z_{n+1} = Q_\Theta(x_{n+1})$$

Another type of inversion approach using a deep learning prior is the so-called deep image prior (DIP) [36]. Rather than using an explicit prior, the deep neural network architecture itself is used as a regularization by restricting the solution space:

$$(2.8) \quad \min_{\Theta} c(\Theta; y, \mathcal{H}) = \|y - \mathcal{H}Q_\Theta(z)\|^2$$

where  $z$  is a random vector. Then, the final solution becomes  $x = Q_{\Theta^*}(z)$  with  $\Theta^*$  being the estimated network parameters. Similarly, generative approaches [37, 5, 39] either estimate the random variable  $z$  from (2.8) by fixing  $\Theta$ , or attempt to estimate both the random  $z$  and the network weight  $\Theta$ .

**3. Main Contributions.** One of the basic assumptions in the aforementioned PLS formulation with a deep learning prior is that the measurement  $y$  is fixed and one is interested in finding the unknown  $x$ . In this paper, we relax the assumption to consider situations where both of them are random samples from joint probability measure  $\pi(x, y)$ . Specifically, we propose a new PLS cost function with a novel deep learning prior as follows:

$$(3.1) \quad c(x, y; \Theta, \mathcal{H}) = \|y - \mathcal{H}x\|^q + \lambda \|G_\Theta(y) - x\|^p$$

with  $p, q \geq 1$ , where  $x, y$  are the random vectors, where  $\Theta, \mathcal{H}$  are the network and measurement system parameters that should be estimated. These parameters can be found by minimizing the average transport cost for all combinations of  $x \in \mathcal{X}$  and  $y \in \mathcal{Y}$  with respect to the joint measure  $\pi(x, y)$ :

$$(3.2) \quad \mathbb{K}(\Theta, \mathcal{H}) := \min_{\pi} \int_{\mathcal{X} \times \mathcal{Y}} c(x, y; \Theta, \mathcal{H}) d\pi(x, y)$$

where the minimum is taken over all joint distributions whose marginal distributions with respect to  $X$  and  $Y$  are  $\mu$  and  $\nu$ , respectively. In (3.1),  $\lambda$  is the regularization term. For simplicity, in the rest of the paper, we assume  $\lambda = 1$ .

Eq. (3.2) is the *primal* form of the optimal transport problem. Now, our goal is to obtain its *dual* formulation using the Kantorovich's dual formula. Although the additive form of the PLS cost in (3.1) makes it difficult to obtain the explicit dual formula, Proposition 3.1 shows that there exists interesting bounds that can be used to minimize the approximation error.

**Proposition 3.1.** *For the given average transportation cost  $\mathbb{K}(\Theta, \mathcal{H})$  of the primal OT problem for with the PLS cost (3.1) with  $p = q = 1$*

$$(3.3) \quad \mathbb{K}(\Theta, \mathcal{H}) = \min_{\pi} \int_{\mathcal{X} \times \mathcal{Y}} \|y - \mathcal{H}x\| + \|G_{\Theta}(y) - x\| d\pi(x, y)$$

let us define a new cost:

$$(3.4) \quad \mathbb{D}(\Theta, \mathcal{H}) := \ell_{\text{cycle}}(\Theta, \mathcal{H}) + \frac{1}{2} \ell_{OT'}(\Theta, \mathcal{H})$$

where

$$(3.5) \quad \ell_{\text{cycle}}(\Theta, \mathcal{H}) = \frac{1}{2} \left\{ \int_{\mathcal{X}} \|x - G_{\Theta}(\mathcal{H}x)\| d\mu(x) + \int_{\mathcal{Y}} \|y - \mathcal{H}G_{\Theta}(y)\| d\nu(y) \right\}$$

$$(3.6) \quad \ell_{OT'}(\Theta, \mathcal{H}) = \frac{1}{2} \left\{ \max_{\varphi} \int_{\mathcal{X}} \varphi(x) d\mu(x) - \int_{\mathcal{Y}} \varphi(G_{\Theta}(y)) d\nu(y) \right. \\ \left. + \max_{\psi} \int_{\mathcal{Y}} \psi(y) d\nu(y) - \int_{\mathcal{X}} \psi(\mathcal{H}x) d\mu(x) \right\}$$

where  $\varphi, \psi$  are 1-Lipschitz functions. Then, the average transportation cost  $\mathbb{K}(\Theta, \mathcal{H})$  of the primal OT problem in (3.2) for  $p = q = 1$  can be approximated by  $\mathbb{D}(\Theta, \mathcal{H})$  with the following error bound:

$$(3.7) \quad |\mathbb{K}(\Theta, \mathcal{H}) - \mathbb{D}(\Theta, \mathcal{H})| \leq \frac{1}{2} \ell_{\text{cycle}}(\Theta, \mathcal{H})$$

and the approximation error becomes zero for  $(\Theta, \mathcal{H})$  such that  $\mathcal{H}G_{\Theta}(y) = y$  and  $G_{\Theta}\mathcal{H}x = x$  for all  $x \in \mathcal{X}, y \in \mathcal{Y}$ .

*Proof.* We first define the optimal joint measure  $\pi^*$  for the primal problem (3.2) with  $p = q = 1$ :

$$\mathbb{K}(\Theta, \mathcal{H}) = \min_{\pi} \int_{\mathcal{X} \times \mathcal{Y}} c(x, y; \Theta, \mathcal{H}) \pi(dx, dy) = \int_{\mathcal{X} \times \mathcal{Y}} c(x, y; \Theta, \mathcal{H}) \pi^*(dx, dy)$$

where  $c(x, y; \Theta, \mathcal{H}) := \|y - \mathcal{H}x\| + \|G_{\Theta}(y) - x\|$ . Using the two forms of the Kantorovich dual formulations in (2.3) and (2.4), we have

$$\begin{aligned} \mathbb{K}(\Theta, \mathcal{H}) &= \int_{\mathcal{X} \times \mathcal{Y}} \|y - \mathcal{H}x\| + \|G_{\Theta}(y) - x\| d\pi^*(x, y) \\ &= \frac{1}{2} \left\{ \max_{\varphi} \int_{\mathcal{X}} \varphi(x) d\mu(x) + \int_{\mathcal{Y}} \varphi^c(y) d\nu(y) + \max_{\psi} \int_{\mathcal{X}} \psi^c(x) d\mu(x) + \int_{\mathcal{Y}} \psi(y) d\nu(y) \right\} \\ &= \frac{1}{2} \left\{ \max_{\varphi} \int_{\mathcal{X}} \varphi(x) d\mu(x) + \int_{\mathcal{Y}} \inf_x \{ \|y - \mathcal{H}x\| + \|G_{\Theta}(y) - x\| - \varphi(x) \} d\nu(y) \right. \\ &\quad \left. + \max_{\psi} \int_{\mathcal{X}} \inf_y \{ \|y - \mathcal{H}x\| + \|G_{\Theta}(y) - x\| - \psi(y) \} d\mu(x) + \int_{\mathcal{Y}} \psi(y) d\nu(y) \right\} \end{aligned}$$

Now, instead of finding the  $\inf_x$ , we choose  $x = G_\Theta(x)$ ; similarly, instead of  $\inf_y$ , we chose  $y = \mathcal{H}x$ . This leads to an upper bound:

$$\begin{aligned} \mathbb{K}(\Theta, \mathcal{H}) &\leq \frac{1}{2} \left\{ \max_{\varphi} \int_{\mathcal{X}} \varphi(x) d\mu(x) - \int_{\mathcal{Y}} \varphi(G_\Theta(y)) d\nu(y) + \int_{\mathcal{Y}} \|y - \mathcal{H}G_\Theta(y)\| d\nu(y) \right. \\ &\quad \left. + \max_{\psi} \int_{\mathcal{Y}} \psi(y) d\nu(y) - \int_{\mathcal{X}} \psi(\mathcal{H}x) d\mu(x) + \int_{\mathcal{X}} \|G_\Theta(\mathcal{H}x) - x\| d\mu(x) \right\} \\ &= \frac{1}{2} \left\{ \max_{\varphi} \int_{\mathcal{X}} \varphi(x) d\mu(x) - \int_{\mathcal{Y}} \varphi(G_\Theta(y)) d\nu(y) + \max_{\psi} \int_{\mathcal{Y}} \psi(y) d\nu(y) - \int_{\mathcal{X}} \psi(\mathcal{H}x) d\mu(x) \right. \\ &\quad \left. + \int_{\mathcal{X}} \|G_\Theta(\mathcal{H}x) - x\| d\mu(x) + \int_{\mathcal{Y}} \|y - \mathcal{H}G_\Theta(y)\| d\nu(y) \right\} \\ &= \ell_{OT'}(\Theta, \mathcal{H}) + \ell_{cycle}(\Theta, \mathcal{H}) \end{aligned}$$

Now, using 1-Lipschitz continuity of the Kantorovich potentials, we have

$$(3.8) \quad -\varphi(G_\Theta(y)) \leq \|G_\Theta(y) - x\| - \psi(y) \leq \|y - \mathcal{H}x\| + \|G_\Theta(y) - x\| - \psi(y)$$

$$(3.9) \quad -\psi(\mathcal{H}x) \leq \|y - \mathcal{H}x\| - \psi(y) \leq \|y - \mathcal{H}x\| + \|G_\Theta(y) - x\| - \psi(y)$$

This leads to the following lower-bound

$$\begin{aligned} \mathbb{K}(\Theta, \mathcal{H}) &\geq \frac{1}{2} \left\{ \max_{\varphi} \int_{\mathcal{X}} \varphi(x) d\mu(x) - \int_{\mathcal{Y}} \varphi(G_\Theta(y)) d\nu(y) + \max_{\psi} \int_{\mathcal{Y}} \psi(y) d\nu(y) - \int_{\mathcal{X}} \psi(\mathcal{H}x) d\mu(x) \right\} \\ &= \ell_{OT'}(\Theta, \mathcal{H}) \end{aligned}$$

By collecting the two bounds, we have

$$\ell_{OT'}(\Theta, \mathcal{H}) \leq \mathbb{K}(\Theta, \mathcal{H}) \leq \ell_{OT'}(\Theta, \mathcal{H}) + \ell_{cycle}(\Theta, \mathcal{H}).$$

which leads to

$$|\mathbb{K}(\Theta, \mathcal{H}) - \mathbb{D}(\Theta, \mathcal{H})| \leq \frac{1}{2} \ell_{cycle}(\Theta, \mathcal{H}).$$

where  $\mathbb{D}(\Theta, \mathcal{H})$  is defined in (3.4). Finally, the approximation error becomes zero when  $\ell_{cycle}(\Theta, \mathcal{H}) = 0$ . This happens for  $(\Theta, \mathcal{H})$  such that  $\mathcal{H}G_\Theta(y) = y$  and  $G_\Theta \mathcal{H}x = x$  for all  $x \in \mathcal{X}, y \in \mathcal{Y}$ .  $\blacksquare$

Recall that the optimal transportation map can be found by minimizing the primal OT cost function  $\mathbb{K}(\Theta, \mathcal{H})$  with respect to  $(\Theta, \mathcal{H})$ :

$$(3.10) \quad \min_{\Theta, \mathcal{H}} \mathbb{K}(\Theta, \mathcal{H})$$

Using Proposition 3.1, this can be equivalently represented by a constrained optimization problem:

$$(3.11) \quad \min_{\Theta, \mathcal{H}} \mathbb{D}(\Theta, \mathcal{H}) \quad \text{subject to } \ell_{cycle}(\Theta, \mathcal{H}) = 0$$

Using Lagrangian multiplier, the constrained optimization problem (3.11) can be converted to an unconstrained optimization problem:

$$(3.12) \quad \min_{\Theta, \mathcal{H}} \mathbb{D}(\Theta, \mathcal{H}) + \alpha \ell_{cycle}(\Theta, \mathcal{H}) \quad \text{or} \quad \min_{\Theta, \mathcal{H}} \ell_{OT'}(\Theta, \mathcal{H}) + \gamma \ell_{cycle}(\Theta, \mathcal{H})$$

where  $\alpha$  is a Lagrangian parameter and  $\gamma = \alpha + \frac{1}{2}$ . Finally, by implementing the Kantorovich potential using CNNs with parameters  $\Phi$  and  $\Xi$ , i.e.  $\varphi := \varphi_\Phi$  and  $\psi := \psi_\Xi$ , we have the the following cycleGAN problem:

$$(3.13) \quad \min_{\Theta, \mathcal{H}} \ell_{OT'}(\Theta, \mathcal{H}) + \gamma \ell_{cycle}(\Theta, \mathcal{H}) = \min_{\Theta, \mathcal{H}} \max_{\Phi, \Xi} \ell(\Theta, \mathcal{H}; \Phi, \Xi)$$

where

$$\ell(\Theta, \mathcal{H}; \Phi, \Xi) = \ell_{GAN}(\Theta, \mathcal{H}; \Phi, \Xi) + \gamma \ell_{cycle}(\Theta, \mathcal{H})$$

where  $\ell_{cycle}(\Theta, \mathcal{H})$  denotes the cycle-consistency loss in (3.5) and  $\ell_{GAN}(\Theta, h; \Phi, \Xi)$  is the GAN loss given by:

$$(3.14) \quad \begin{aligned} \ell_{GAN}(\Theta, \mathcal{H}; \Phi, \Xi) = & \int_{\mathcal{X}} \varphi_\Phi(x) d\mu(x) - \int_{\mathcal{Y}} \varphi_\Phi(G_\Theta(y)) d\nu(y) \\ & + \int_{\mathcal{Y}} \psi_\Xi(y) d\nu(y) - \int_{\mathcal{X}} \psi_\Xi(\mathcal{H}x) d\mu(x) \end{aligned}$$

Here, the Kantorovich 1-Lipschitz potentials  $\varphi := \varphi_\Phi$  and  $\psi := \psi_\Xi$  correspond to the W-GAN discriminators. Specifically,  $\varphi_\Phi$  tries to find the difference between the true image  $x$  and the generated image  $G_\Theta(y)$ , whereas  $\psi := \psi_\Xi$  attempts to find the fake measurement data that are generated by the synthetic measurement procedure  $\mathcal{H}x$ .

Although we call our formulation using (3.13) as cycleGAN, (3.13) has very important advantage compared to the standard cycleGAN [42]. More specifically, the standard cycleGAN [42] usually requires two generators in the form of deep neural networks. On the other hand, our formulation often requires a single generator using a deep neural network, if the other generator is given by the forward model  $\mathcal{H}x$ . This significantly reduces the number of weights, which makes the training much more stable. While we only consider  $p = q = 1$  due to the inequalities (3.8) and (3.9) for 1-Lipschitz  $\varphi$  and  $\psi$ , the use of the general PLS cost would be interesting, and it may lead to an interesting variation of the cycleGAN architecture. This could be done using a regularized version of OT [29].

**3.1. Implications to Inverse Problems.** Before we conclude this section, we discuss the implication of our cycleGAN formulation from ad general inverse problem perspective. Recall that an ill-posed inverse problem  $y = \mathcal{H}x$  can have many solutions. Thus, the main motivation of the classical PLS approach in Section 2.2 is to introduce a penalty term for choosing the solution  $x$ , which is most likely based on the prior distribution of data (see Fig. 1(a)). This reduces the feasible sets, which may mitigate the ill-posedness. On the other hand, the new PLS cost in (3.1) provides another way to resolve the ambiguity of the feasible solutions. Specifically, if we define a *single-valued* function  $G_\Theta(y)$  and impose the constraint  $x = G_{\Theta^*}(y)$

with the learned parameter  $\Theta^*$ , many of the feasible solutions for  $y = \mathcal{H}x$  can be pruned as shown in Fig. 1(b). Therefore, this provides another way of mitigating the ill-posedness.

Given this perspective, the critical question is how to determine the optimal parameter  $\Theta^*$ . This is where the optimal transport theory comes into play. Specifically, our cycleGAN formulation in (3.13) address the problem of finding the parameter  $\Theta^*$ . In particular, when the cycle-consistency term becomes zero, we have

$$(3.15) \quad \ell_{cycle}(\Theta^*) = 0 \implies y = \mathcal{H}x, \quad x = G_{\Theta^*}(y)$$

Therefore,  $G_{\Theta^*}$  can be an inverse of the forward operator  $\mathcal{H}$ . This is the main motivation for using the new penalty function in our formulation.

Another important advantage of the proposed method is that the unknown image  $x$  can be obtained as an output of the feedforward neural network  $G_{\Theta}(y)$  for the given measurement  $y$ . This makes the inversion procedure much simpler. One may say that the PLS cost function for the DIP in (2.8) can produce a different variation of unsupervised learning. However, the resulting formulation is not a feed-forward neural network. Specifically, the primal problem of the OT problem with respect to the DIP cost in (2.8) is given by

$$(3.16) \quad \min_{\pi} \int_{\mathcal{X} \times \mathcal{Z}} \|y - \mathcal{H}G_{\Theta}(z)\| d\pi(x, z)$$

where we consider  $y$  and  $z$  as random variable and we use non-squared norm for simplicity. This leads to the following duality:

$$\min_{\Theta} \min_{\pi} \int_{\mathcal{X} \times \mathcal{Z}} \|y - \mathcal{H}G_{\Theta}(z)\| d\pi(x, z) = \min_{\Theta} \max_{\psi} \int_{\mathcal{Y}} \psi(y) d\nu(y) - \int_{\mathcal{Z}} \psi(\mathcal{H}G_{\Theta}(z)) d\eta(z).$$

where  $\psi$  is a 1-Lipschitz function. Although this is a nice way of pretraining deep image prior model using unmatched training data set, the final image estimate still comes from the following optimization problem:

$$x = G_{\Theta}(z^*) \quad \text{where} \quad z^* = \arg \min_z \|y - \mathcal{H}G_{\Theta}(z)\|$$

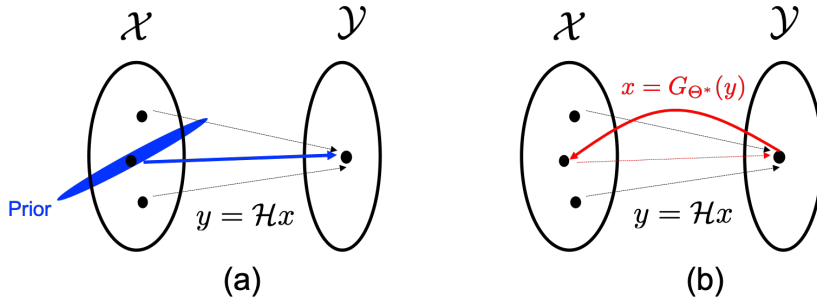


**Figure 1.** Two strategies for resolving ambiguities in the feasible solutions in an ill-posed inverse problem. (a) Classical PLS approach using a close form prior distribution, and (b) our PLS approach using an inverse mapping to define a prior.

where  $\Theta^*$  is the estimated network parameters from previous training step. This is equivalent to deep generator model [5], but this is not useful in designing a feed-forward neural network in an unsupervised manner.

**4. Experimental Results.** In this section, we show that the proposed cycleGAN architecture is quite general and can be used for various applications. Among many potential applications, here we mainly discuss accelerated MRI, super-resolution microscopy, and low-dose CT problems. It turns out that each problem leads to a unique cycleGAN architecture.

**4.1. Accelerated MRI.** In accelerated magnetic resonance imaging (MRI), the goal is to recover high-quality MR images from sparsely sampled  $k$ -space data to reduce the acquisition time. This problem has been extensively studied using compressed sensing [23], but recently, deep learning approaches have been the main research interest due to their excellent performance and significantly reduced run-time complexity [11, 12].

A standard deep learning method for accelerated MRI is based on supervised learning, where the MR images from fully sampled  $k$ -space data are used as references and subsampled  $k$ -space data are used as the input for the neural network for training. Unfortunately, in accelerated MRI, the acquisition of high-resolution fully sampled  $k$ -space data takes significant long time, and often requires changes of the standard acquisition protocols. Therefore, collecting sufficient amount of training data is a major huddle in practice, and the need for unsupervised learning without matched reference data is increasing.

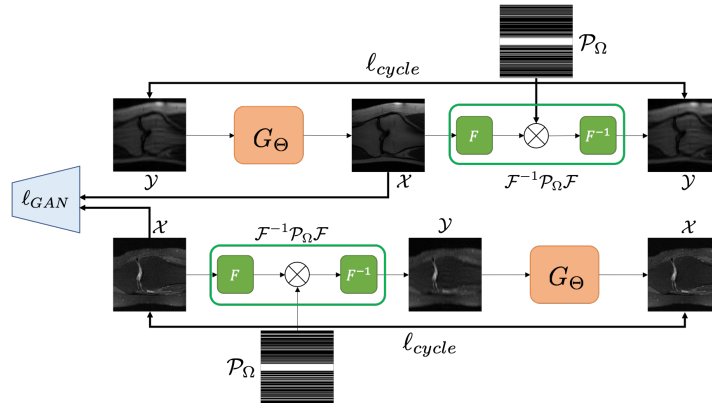


**Figure 2.** Proposed cycleGAN architecture for accelerated MRI with 1-D downsampling patterns.

In accelerated MRI, the forward measurement model can be described as

$$(4.1) \quad \hat{x} = \mathcal{P}_\Omega \mathcal{F}x + w$$

where  $\mathcal{F}$  is the 2-D Fourier transform and  $\mathcal{P}_\Omega$  is the projection to  $\Omega$  that denotes  $k$ -space sampling indices. To implement every step of the algorithm as an image domain processing, (4.1) can be converted to the image domain forward model by applying the inverse Fourier transform:

$$(4.2) \quad y = \mathcal{F}^{-1} \mathcal{P}_\Omega \mathcal{F}x + \mathcal{F}^{-1}w$$

This results in the following cost function for the PLS formulation:

$$(4.3) \quad c(x, y; \Theta) = \|y - \mathcal{F}^{-1} \mathcal{P}_\Omega \mathcal{F} x\| + \|G_\Theta(y) - x\|$$

One of the important considerations in designing the cycleGAN architecture for accelerated MRI is that the sampling mask  $\Omega$  is known so that the forward mapping for the inverse problem is deterministic. This implies that the forward path has no uncertainty and we do not need to estimate  $\mathcal{H} = \mathcal{F}^{-1} \mathcal{P}_\Omega \mathcal{F}$ . Therefore, the maximization of the discriminator  $\psi_\Xi$  in (3.13) with respect to  $\Xi$  does not effect the generator  $G_\Theta$ . Therefore, the discriminator  $\psi_\Xi$  can be neglected.

The schematic diagram of the resulting cycleGAN architecture is illustrated in Fig. 2, whose generator and discriminator architectures are shown in Fig. 3. Note that we just need a single generator and discriminator, as discussed before. For GAN implementation, we use the W-GAN in (3.14) with the Lipschitz penalty loss [10] to ensure that the Kantorovich potential becomes 1-Lipschitz.

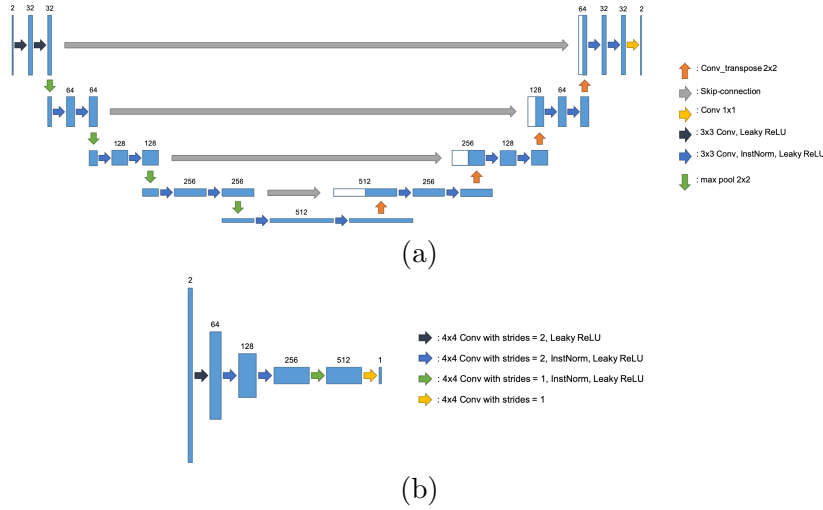


**Figure 3.** Proposed network architecture for (a) generator and (b) discriminator in accelerated MRI.

We use dataset for fastMRI challenge [40] for our experiments. This dataset is composed of MR images of knees. We extracted 3500 MR images from fastMRI single coil validation set. Then, 3000 slices are used for training/evaluation, and 500 slices are used for test. These MR images are fully sampled images, so we make undersampled images by a randomly subsampling k-space lines. The acceleration factor is four, and autocalibration signal (ACS) region contains 4% of k-space lines. Each slice is normalized by standard deviation of the magnitude of each slice. To handle complex values of data, we concatenate real and imaginary values along the channel dimension. Each slice has different size, so we use only single batch. The images are center-cropped to the size of  $320 \times 320$ , and then the peak signal-to-noise ratio (PSNR) and structural similarity index (SSIM) values are calculated. Here, the PSNR and SSIM are defined as

$$\text{PSNR} = 20 \log_{10} \left( \frac{n \|x^*\|_\infty}{\|x - x^*\|_2} \right)$$

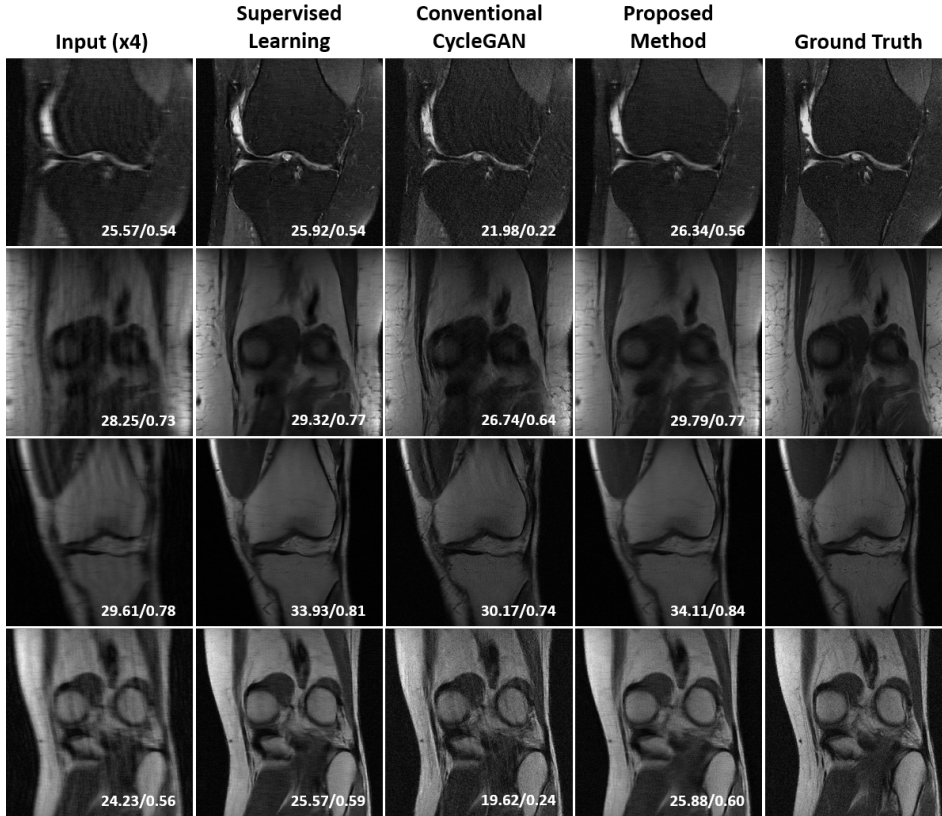


**Figure 4.** Unsupervised learning results for accelerated MRI using proposed cycleGAN. The values in the corners are PSNR/SSIM values for each image.

and

$$\text{SSIM} = \frac{(2\mu_x\mu_{x^*} + c_1)(2\sigma_{xx^*} + c_2)}{(\mu_x^2 + \mu_{x^*}^2 + c_1)(\sigma_x^2 + \sigma_{x^*}^2 + c_2)},$$

where  $x$  and  $x^*$  denote the reconstructed images and ground truth, respectively,  $n$  is the number of pixels,  $\mu_x$  is an average of  $x$ ,  $\sigma_x^2$  is a variance of  $x$  and  $\sigma_{xx^*}$  is a covariance of  $x$  and  $x^*$ , and  $c_1, c_2$  are two variables to stabilize the division.

We use U-Net generator to reconstruct fully sampled MR images from undersampled MR images as shown in Fig. 3(a). Our generator consists of  $3 \times 3$  convolution, Instance normalization, and leaky ReLU operation. Also, there are skip-connection and pooling layers. At the last convolution layer, we do not use any operation. Our discriminator is same as the discriminator of original CycleGAN. We use PatchGAN [16], so the discriminator classifies inputs at patch scales. The discriminator also consists of convolution layer, instance normalization, and leaky ReLU operation as shown in Fig. 3(b). We use Adam optimizer to train our network, with momentum parameters  $\beta_1 = 0.5$ ,  $\beta_2 = 0.9$ , and learning rate of 0.0001. The discriminator is updated 5 times for every generator updates. We use batch size of 1, and trained our network during 100 epochs. Our code was implemented by TensorFlow.

The reconstruction results in Fig. 4 and quantitative comparison results for all test sets in

Table 1 clearly show that the proposed unsupervised learning method using the novel cycleGAN architecture with a single generator successfully recovered fine details without matched references. Moreover, the performance is even better than that of the standard cycleGAN, and it is comparable with that of supervised learning.

**Table 1**

*Quantitative comparison for various algorithms on 500 test sets of fastMRI data.*

Metric	Input ( $\times 4$ )	Supervised Learning	Conventional CycleGAN	Proposed Method
PSNR (dB)	26.81	27.96	25.01	<b>28.17</b>
SSIM	0.6419	0.6419	0.4689	<b>0.6550</b>

**4.2. Single-molecule Localization Microscopy.** Single-molecule localization microscopy methods, such as STORM [32] and (F)PALM [14, 4], utilize sparse activation of photo-switchable fluorescent probes in both temporal and spatial domains. Each activated probe is assumed as an ideal point source so that one can achieve sub-pixel accuracy on the order of tens of nanometers for the estimated location of each probe [32, 4, 35, 13, 28]. In general, reconstruction of sub-cellular structures relies on numerous localized probes, which leads to relatively long acquisition time. To reduce the acquisition time, high density imaging with sparsity regularized deconvolution approaches such as CSSTORM [43] (Compressed sensing STORM) and deconvolution-STORM (deconSTORM)[26] have been investigated. Recently, CNN approaches such as DeepSTORM [27] have been extensively studied as fast and high-performance alternatives. Unfortunately, the existing CNN approaches usually require matched high-resolution images for supervised training, which is not practical.

To address the problem, we are interested in developing unsupervised learning approach for super-resolution microscopy. Mathematically, a blurred measurement can be described as

$$(4.4) \quad y = h * x + w ,$$

where  $h$  is the PSF. Here, we consider the blind deconvolution problem where both the unknown PSF  $h$  and the image  $x$  should be estimated. This results in the following cost function for the PLS formulation:

$$(4.5) \quad c(x, y; \Theta, h) = \|y - h * x\| + \|G_{\Theta}(y) - x\|.$$

The corresponding cycleGAN architecture is illustrated in Fig. 5. In contrast to the standard cycleGAN approaches that require two deep generators, the proposed cycleGAN approach needs only a single deep generator, and the blur generator is implemented using a linear convolution layer corresponding to the unknown PSF. It is important to note that unlike the accelerated MRI problem in the previous section, we still need two discriminators, since both linear and deep generators should be estimated. Still the simplicity of the proposed cycleGAN architecture compared to the standard cycleGAN significantly improves the robustness of network training.

The network architecture of the high resolution image generator  $G_{\Theta}$  from the low-resolution image is a modified U-net [31] as shown in Fig 6. Our U-net consists of two parts: encoder and decoder. For both encoder and decoder, batch normalization [15] and ReLU layers follow

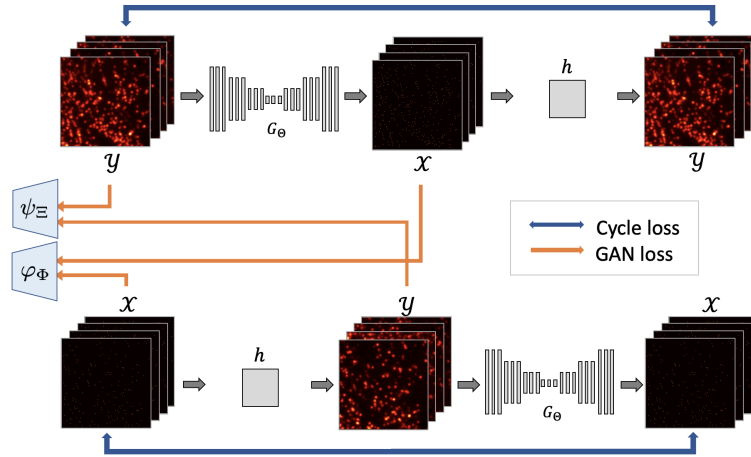


**Figure 5.** Proposed cycleGAN architecture with a blur kernel for deconvolution microscopy. Here,  $G_{\Theta}$  denotes the CNN-based low-resolution to high-resolution generator. The blur generator is composed of a linear blur kernel  $h$ .

every convolution layer except the last one. At the last layer, only batch normalization layer follows the convolution layer. Throughout the whole network, the convolutional kernel size is  $3 \times 3$  with no stride. A max pooling layer exist at the encoder part with kernel size  $2 \times 2$  and stride 2. The number of the channel increases and becomes the maximum at the end of encoder part. In this paper, the maximum number of the channel is 300.

For the second generator, a single 2D convolution layer is used. This layer is to the model of 2D PSF to generate blurry low-resolution image from high resolution input. The kernel size of the single 2D convolution layer is set to  $10 \times 10$ . As for the discriminators, we used simple convolution-based architecture as shown in Fig 7. It has three layer-blocks. Each block consists of 2D convolution - batch normalization - ReLU. Throughout the whole network, the convolutional kernel size is  $5 \times 5$  with stride 3. After all three blocks, fully connected layer followed by a sigmoid function is added to generator scalar value decision between 0 and 1.

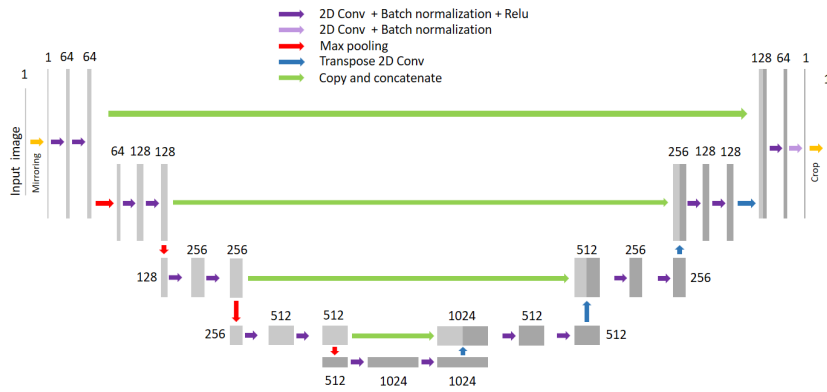


**Figure 6.** A modified 2D U-net architecture used for our high-resolution image generator.

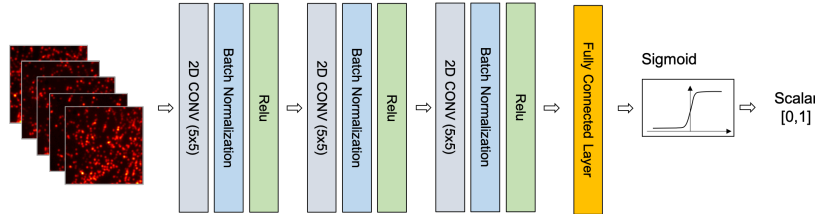


Figure 7. Discriminator architecture.

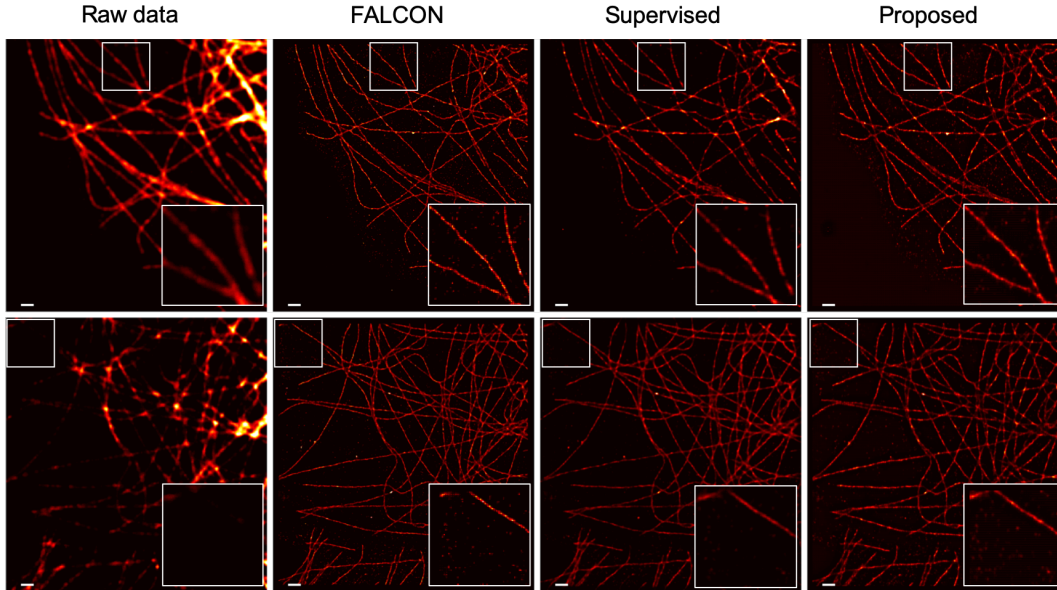


Figure 8. Reconstruction results by various methods. (First column) low resolution raw data from SMLM, (second column) FALCON reconstruction, (third column) supervised learning results, and (the last column) unsupervised reconstruction results by the proposed cycleGAN. The image within white box is magnified by 2 times. The white scale bar on the left lower side of each images is  $1\mu\text{m}$ .

For our experiments, three real single molecule localization microscope (SMLM) image sets obtained from  $\alpha$ -tubulin subunits of microtubules are used. Among the three data sets, the first data set composed of 500 frames of  $128 \times 128$  image was used for training. The second data sets was composed of 1000 frames of  $128 \times 128$  measurement, and the third data set was composed of 2000 frame of  $128 \times 128$  measurement. These two data set were used for test. Using data augmentation by vertical and horizontal flipping, we increased the training data set size by four times. Among them, 1800 frames were used for training, and the other 200 frames for validation. From these low resolution measurements, high resolution images of  $256 \times 256$  were reconstructed using neural networks. To generate the larger size images, the low resolution images are first upsampled by four times (i.e.  $2 \times 2$  upsampling) to be used as a network input. To overcome GPU memory limitation, the input images were divided into  $128 \times 128$  size patches. We normalized the scale of the whole input images to  $[0,1]$ . We employed Adam optimizer [20] and the learning rate was set to 0.0001 (constant value). The

number of epoch was 50, and 1800 optimization were done per each epoch. Due to a lack of matched label data, we use the random point set images as high resolution data set in our unsupervised training, and our neural network was trained to follow the distribution of random point sets.

As for comparison, we employed a state-of-the-art method called FAsT Localization algorithm based on a CONTinuous-space formulation (FALCON) [25], and DeepSTORM [27] that uses the U-Net architecture in a supervised learning framework. For supervised training, we used the high resolution images from FALCON as label data.

Fig. 8 shows the comparison results for two test data set. To generate the images, each frame of the SMLM was processed with the super-resolution algorithm, after which all the temporal frames are averaged. As shown in Fig. 8, all methods provide the comparable reconstruction results while FALCON image looks sharper since it is based on the centroid coordinate estimation by Talyor series expansion, rather than image deconvolution. The reconstruction results by the proposed method provides comparable results with supervised learning approach. To quantify the resolution improvement, we use the Fourier ring correlation (FRC) [21], which is a widely used criterion for resolution estimation. Interestingly, the FRC resolution shown in Table 2 showed that the proposed method provides the best FRC resolution.

**Table 2**

*Quantitative comparison of reconstruction resolution using FRC by various algorithms on the two test data sets. The unit of the FRC is nm and the value shows average and standard deviation.*

Test data	FALCON	Supervised Learning	Proposed Method
Test set 2	45.62 ± 12.43	41.11 ± 10.15	<b>32.49 ± 11.62</b>
Test set 3	50.33 ± 8.52	46.09 ± 6.87	<b>31.63 ± 6.24</b>

**4.3. Image Denoising in X-Ray CT.** X-Ray CT retains a potential risk of cancer, induced by radiation exposure. However, the low dose CT (LDCT) reduces signal-to-noise ratio (SNR) in the obtained images compared to standard-dose CT (SDCT). Therefore, extensive studies have been carried out to achieve reduced noise level in LDCT images. Although model-based iterative reconstruction (MBIR) methods [3, 30, 34, 7] have been developed to address the problem, the method suffers from long reconstruction time due to iterative procedure.

Recently, deep learning approaches demonstrated improved performance compared to the conventional methods [19, 17, 8]. Unfortunately, it is difficult to get paired LDCT and SDCT data in clinical practice. Therefore, the approach based on a unsupervised learning is suitable for the practical application.

Since the noise patterns in LDCT contains many streaking and physics-dependent artifacts, it is difficult to model the noise as simple Gaussian noise model. Therefore, rather than modeling the noise with specific closed-form statistics, we assume that the LDCT image is given by the nonlinear mapping from the SDCT image. This is modeled by another neural network  $F_{\mathcal{H}}$ . This results in the following cost function for the PLS formulation:

$$(4.6) \quad c(x, y; \Theta, \Gamma) = \|y - F_{\mathcal{H}}(x)\| + \|G_{\Theta}(y) - x\|.$$

The resulting architecture of cycleGAN is shown in Fig. 9. Here, two generators and two

discriminators are used, since the noise process should be also estimated using the neural network. In fact, the resulting architecture is basically the same as the standard CycleGAN [42].

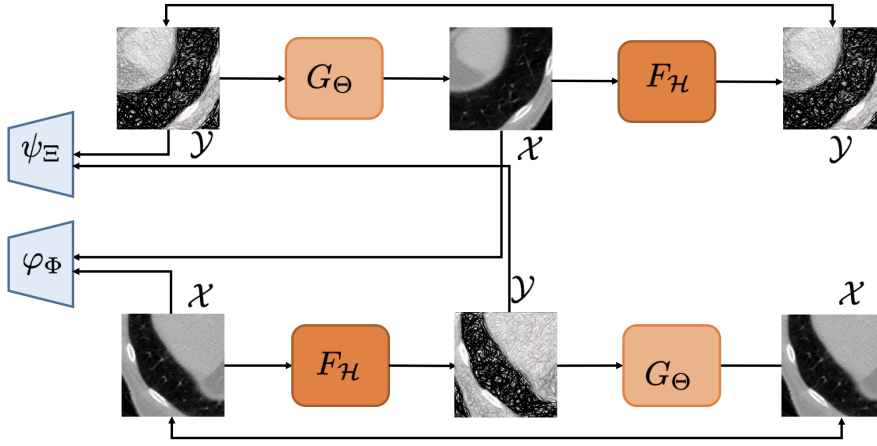


Figure 9. Proposed cycleGAN architecture for CT image denoising

The generators  $G_\Theta$  and  $F_{\mathcal{H}}$  are implemented using the U-net structure as shown in Fig. 10. They have 3 stages of pooling. The feature map at each stage is extracted by convolutional blocks, which consist of  $3 \times 3$  convolution, instance normalization, and ReLU. Also, there is skip connection for every stage. The  $128 \times 128$  patch images cropped from original image are used as inputs for the generator. For the discriminators, the architecture of PatchGAN as shown in Fig. 11 was used. The network gets  $128 \times 128$  patch image as an input, and decides whether they are real or generated from the generator. The discriminator consists of  $4 \times 4$  convolution, Instance normalization and ReLU operation. Adam optimizer with the batch size of 20 was used for training. Total training epoch was 100.

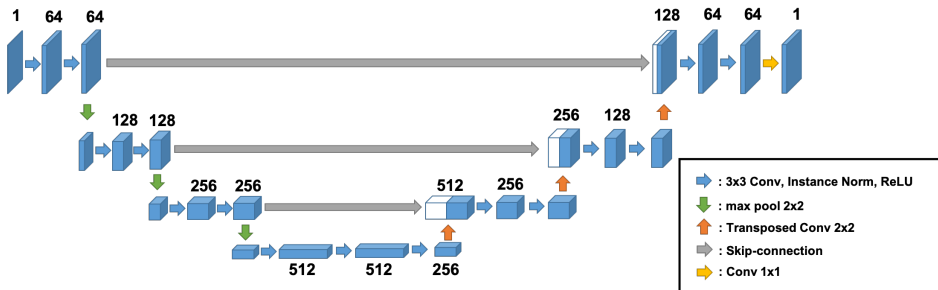


Figure 10. U-net architecture for generator  $G_{AB}$  and  $G_{BA}$  in the proposed cycleGAN

The abdominal CT dataset provided in Low Dose CT Grand Challenge of American Association of Physicists in Medicine (AAPM) was used for the experiments. LDCT and SDCT dataset, which contains 3000 images for each set, are used for training. 500 images for

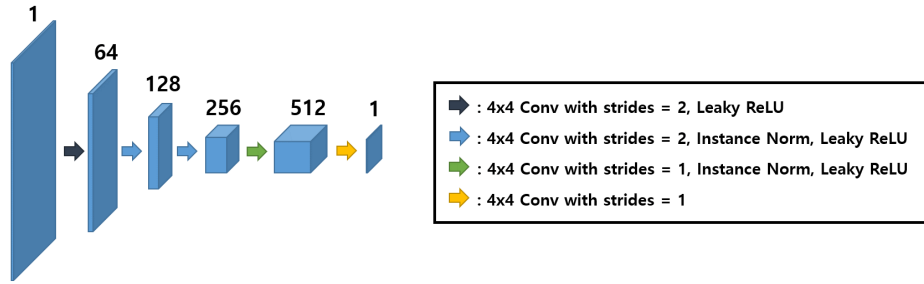


Figure 11. Network architecture for discriminator  $G_{\Theta}$  and  $F_{\mathcal{H}}$  in the proposed cycleGAN

each LDCT and SDCT images are chosen for validation set. Another 500 images for each set are selected for test. In training procedure for the cycleGAN, LDCT and SDCT data sets are shuffled to be unpaired. In the evaluation procedure, the paired LDCT and SDCT data are used to obtain PSNR and SSIM to quantify the performance.

Table 3 and Fig.12 demonstrates that the denoising was successfully achieved by the cycleGAN. Also, it is remarkable that the performance of the cycleGAN is comparable with that of supervised learning, even though any paired data was used for training.

Table 3

Quantitative performance comparison using 500 test sets of CT data

Metric	Input	Supervised Learning	Suggested cycleGAN
PSNR (dB)	33.48	37.52	37.45
SSIM	0.7449	0.8759	0.8718

**5. Conclusions.** In this paper, we presented a general design principle for a cycleGAN architecture for various inverse problems. Specifically, the proposed architecture was obtained from Kantorovich’s dual OT problems, where a novel PLS cost with the data consistency and deep learning prior is used as a transportation cost. As proofs of concept, we designed novel cycleGAN architectures for accelerated MRI, super-resolution microscopy, low-dose CT reconstruction problems, providing accurate reconstruction results without any matched reference data. Given the generality of our design principle, we believe that our method can be an important platform for unsupervised learning for inverse problems.

## REFERENCES

- [1] H. K. AGGARWAL, M. P. MANI, AND M. JACOB, *MoDL: Model-based deep learning architecture for inverse problems*, IEEE transactions on medical imaging, 38 (2018), pp. 394–405.
- [2] M. ARJOVSKY, S. CHINTALA, AND L. BOTTOU, *Wasserstein GAN*, arXiv preprint arXiv:1701.07875, (2017).
- [3] M. BEISTER, D. KOLDITZ, AND W. A. KALENDER, *Iterative reconstruction methods in x-ray ct*, Physica Medica, 28 (2012), pp. 94 – 108.

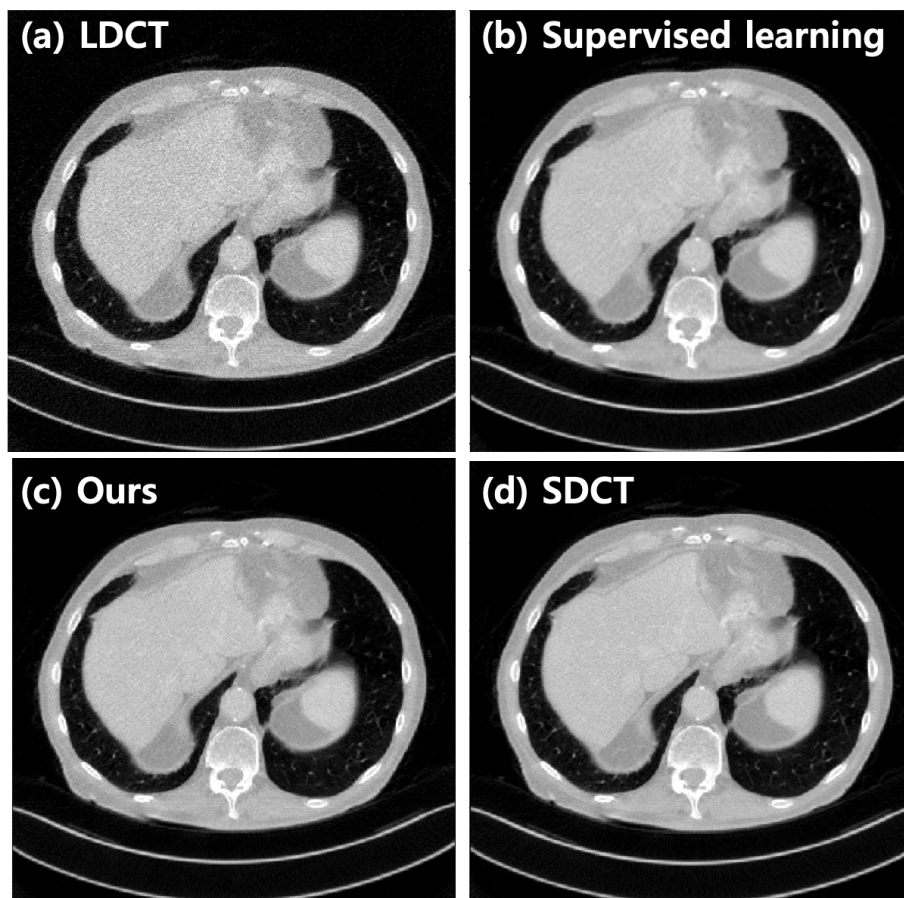


**Figure 12.** Qualitative comparison of denoising performance. (a) LDCT image, and denoising results by (b) supervised learning, (c) our cycleGAN, and (d) SDCT image. CT images are displayed with  $(-850, 900)$ [HU] window.

- [4] E. BETZIG, G. H. PATTERSON, R. SOUGRAT, O. W. LINDWASSER, S. OLENYCH, J. S. BONIFACINO, M. W. DAVIDSON, J. LIPPINCOTT-SCHWARTZ, AND H. F. HESS, *Imaging intracellular fluorescent proteins at nanometer resolution*, Science, 313 (2006), pp. 1642–1645.
- [5] A. BORA, A. JALAL, E. PRICE, AND A. G. DIMAKIS, *Compressed sensing using generative models*, in Proceedings of the 34th International Conference on Machine Learning-Volume 70, JMLR. org, 2017, pp. 537–546.
- [6] S. CHAUDHURI, R. VELMURUGAN, AND R. RAMESHAN, *Blind deconvolution methods: A review*, in Blind Image Deconvolution, Springer, 2014, pp. 37–60.
- [7] G.-H. CHEN, J. TANG, AND S. LENG, *Prior image constrained compressed sensing (piccs): A method to accurately reconstruct dynamic ct images from highly undersampled projection data sets*, Medical Physics, 35 (2008), pp. 660–663.
- [8] H. CHEN, Y. ZHANG, M. K. KALRA, F. LIN, Y. CHEN, P. LIAO, J. ZHOU, AND G. WANG, *Low-dose ct with a residual encoder-decoder convolutional neural network*, IEEE Transactions on Medical Imaging, 36 (2017), pp. 2524–2535.
- [9] I. GOODFELLOW, J. POUGET-ABADIE, M. MIRZA, B. XU, D. WARDE-FARLEY, S. OZAIR, A. COURVILLE, AND Y. BENGIO, *Generative adversarial nets*, in Advances in neural information processing systems,

- 2014, pp. 2672–2680.
- [10] I. GULRAJANI, F. AHMED, M. ARJOVSKY, V. DUMOULIN, AND A. C. COURVILLE, *Improved training of Wasserstein GANs*, in Advances in neural information processing systems, 2017, pp. 5767–5777.
  - [11] K. HAMMERNIK, T. KLATZER, E. KOBLER, M. P. RECHT, D. K. SODICKSON, T. POCK, AND F. KNOLL, *Learning a variational network for reconstruction of accelerated MRI data*, Magnetic resonance in medicine, 79 (2018), pp. 3055–3071.
  - [12] Y. HAN AND J. C. YE, *k-Space Deep Learning for Accelerated MRI*, IEEE Transactions on Medical Imaging (in press), also available as arXiv preprint arXiv:1805.03779, (2019).
  - [13] R. HENRIQUES, M. LELEK, E. F. FORNASIERO, F. VALTORTA, C. ZIMMER, AND M. M. MHLANGA, *Quickpalm: 3d real-time photoactivation nanoscopy image processing in imagej*, Nat. Methods, 7 (2010), pp. 339–340.
  - [14] S. T. HESS, T. P. GIRIRAJAN, AND M. D. MASON, *Ultra-high resolution imaging by fluorescence photoactivation localization microscopy*, Biophys. J., 91 (2006), p. 4258.
  - [15] S. IOFFE AND C. SZEGEDY, *Batch normalization: Accelerating deep network training by reducing internal covariate shift*, arXiv preprint arXiv:1502.03167, (2015).
  - [16] P. ISOLA, J.-Y. ZHU, T. ZHOU, AND A. A. EFROS, *Image-to-image translation with conditional adversarial networks*, in Proceedings of the IEEE conference on computer vision and pattern recognition, 2017, pp. 1125–1134.
  - [17] E. KANG, W. CHANG, J. YOO, AND J. C. YE, *Deep convolutional framelet denoising for low-dose ct via wavelet residual network*, IEEE Transactions on Medical Imaging, 37 (2018), pp. 1358–1369.
  - [18] E. KANG, H. J. KOO, D. H. YANG, J. B. SEO, AND J. C. YE, *Cycle-consistent adversarial denoising network for multiphase coronary CT angiography*, Medical physics, 46 (2019), pp. 550–562.
  - [19] E. KANG, J. MIN, AND J. C. YE, *A deep convolutional neural network using directional wavelets for low-dose X-ray CT reconstruction*, Medical physics, 44 (2017).
  - [20] D. P. KINGMA AND J. BA, *Adam: A method for stochastic optimization*, arXiv preprint arXiv:1412.6980, (2014).
  - [21] S. KOHO, G. TORTAROLO, M. CASTELLO, T. DEGUCHI, A. DIASPRO, AND G. VICIDOMINI, *Fourier ring correlation simplifies image restoration in fluorescence microscopy*, Nature Communications, 10 (2019), pp. 2041–1723.
  - [22] Y. LU, Y.-W. TAI, AND C.-K. TANG, *Conditional cyclegan for attribute guided face image generation*, arXiv preprint arXiv:1705.09966, (2017).
  - [23] M. LUSTIG, D. DONOHO, AND J. M. PAULY, *Sparse MRI: The application of compressed sensing for rapid MR imaging*, Magn. Reson. Med., 58 (2007), pp. 1182–1195.
  - [24] J. G. MCNALLY, T. KARPOVA, J. COOPER, AND J. A. CONCHELLO, *Three-dimensional imaging by deconvolution microscopy*, Methods, 19 (1999), pp. 373–385.
  - [25] J. MIN, C. VONESCH, H. KIRSHNER, L. CARLINI, N. OLIVIER, S. HOLDEN, S. MANLEY, J. C. YE, AND M. UNSER, *Falcon: fast and unbiased reconstruction of high-density super-resolution microscopy data*, Scientific Reports, 4 (2014), pp. 2045–2322.
  - [26] E. A. MUKAMEL, H. BABCOCK, AND X. ZHUANG, *Statistical deconvolution for superresolution fluorescence microscopy*, Biophys. J., 102 (2012), pp. 2391–2400.
  - [27] E. NEHME, L. E. WEISS, T. MICHAELI, AND Y. SHECHTMAN, *DeepSTORM: super-resolution single-molecule microscopy by deep learning*, Optica, 5 (2018), pp. 458–464.
  - [28] R. PARTHASARATHY, *Rapid, accurate particle tracking by calculation of radial symmetry centers*, Nat. Methods, 9 (2012), pp. 724–726.
  - [29] G. PEYRÉ, M. CUTURI, ET AL., *Computational optimal transport*, Foundations and Trends in Machine Learning, 11 (2019), pp. 355–607.
  - [30] S. RAMANI AND J. A. FESSLER, *A splitting-based iterative algorithm for accelerated statistical x-ray ct reconstruction*, IEEE Transactions on Medical Imaging, 31 (2012), pp. 677–688.
  - [31] O. RONNEBERGER, P. FISCHER, AND T. BROX, *U-net: Convolutional networks for biomedical image segmentation*, CoRR, abs/1505.04597 (2015), <http://arxiv.org/abs/1505.04597>, <https://arxiv.org/abs/1505.04597>.
  - [32] M. J. RUST, M. BATES, AND X. ZHUANG, *Sub-diffraction-limit imaging by stochastic optical reconstruction microscopy STORM*, Nat. Methods, 3 (2006), pp. 793–796.
  - [33] P. SARDER AND A. NEHORAI, *Deconvolution methods for 3-D fluorescence microscopy images*, IEEE

- Signal Processing Magazine, 23 (2006), pp. 32–45.
- [34] E. Y. SIDKY AND X. PAN, *Image reconstruction in circular cone-beam computed tomography by constrained, total-variation minimization*, Physics in Medicine and Biology, 53 (2008), pp. 4777–4807.
  - [35] C. S. SMITH., N. JOSEPH., B. RIEGER., AND K. A. LIDKE, *Fast, single-molecule localization that achieves theoretically minimum uncertainty*, Nat. Methods, 7 (2010), pp. 373–375.
  - [36] D. ULYANOV, A. VEDALDI, AND V. LEMPITSKY, *Deep image prior*, in Proceedings of the IEEE Conference on Computer Vision and Pattern Recognition, 2018, pp. 9446–9454.
  - [37] D. VAN VEEN, A. JALAL, M. SOLTANOLKOTABI, E. PRICE, S. VISHWANATH, AND A. G. DIMAKIS, *Compressed sensing with deep image prior and learned regularization*, arXiv preprint arXiv:1806.06438, (2018).
  - [38] C. VILLANI, *Optimal transport: old and new*, vol. 338, Springer Science & Business Media, 2008.
  - [39] Y. WU, M. ROSCA, AND T. LILICRAP, *Deep compressed sensing*, arXiv preprint arXiv:1905.06723, (2019).
  - [40] J. ZBONTAR, F. KNOLL, A. SRIRAM, M. J. MUCKLEY, M. BRUNO, A. DEFazio, M. PARENTE, K. J. GERAS, J. KATSNELSON, H. CHANDARANA, ET AL., *fastMRI: An open dataset and benchmarks for accelerated MRI*, arXiv preprint arXiv:1811.08839, (2018).
  - [41] K. ZHANG, W. ZUO, S. GU, AND L. ZHANG, *Learning deep CNN denoiser prior for image restoration*, in Proceedings of the IEEE conference on computer vision and pattern recognition, 2017, pp. 3929–3938.
  - [42] J.-Y. ZHU, T. PARK, P. ISOLA, AND A. A. EFROS, *Unpaired image-to-image translation using cycle-consistent adversarial networks*, in Proceedings of the IEEE international conference on computer vision, 2017, pp. 2223–2232.
  - [43] L. ZHU, W. ZHANG, D. ELNATAN, AND B. HUANG, *Faster storm using compressed sensing*, Nat. Methods, 9 (2012), pp. 721–723.